

Wang, H., Hernández-Jiménez, F., Lungu, M., Huang, Z., Yang, Y., Wang, J. & Yang, Y. (2018). Critical comparison of electrostatic effects on hydrodynamics and heat transfer in a bubbling fluidized bed with a central jet. *Chemical Engineering Science*, vol. 191, pp. 156–168.

DOI: 10.1016/j.ces.2018.06.069



# Critical comparison of electrostatic effects on hydrodynamics and heat transfer in a bubbling fluidized bed with a central jet

Haotong Wang [a], Fernando Hernández Jiménez [b], Musango Lungu [a,c], Zhengliang Huang [a], Yao Yang* [a], Jingdai Wang [a], Yongrong Yang [a]

[a] *Zhejiang Provincial Key Laboratory of Advanced Chemical Engineering Manufacture Technology, College of Chemical and Biological Engineering, Zhejiang University, Hangzhou 310027, China*

[b]*Departamento de Ingeniería Térmica y de Fluidos, Universidad Carlos III de Madrid, ISE Research Group, Avda. Universidad, 30, 28911 Leganes, Madrid, Spain*

[c]*Chemical Engineering Department, School of Mines and Mineral Sciences, Copperbelt University, Kitwe, Copperbelt province 10101, Zambia*

*To whom should be corresponded. Tel.:+86-571-87951227 Fax: +86-571-87951227 Email: yao_yang@zju.edu.cn

**Abstract**

In many industrial process, electrostatic charges are inevitable. and affect the hydrodynamic behavior and heat transfer ability of chemical equipment. A comprehensive study of the electrostatic effect on bubble behavior, particle fluctuation velocity and heat transfer coefficient in the fluidized bed with a central jet has been evaluated in this paper by Eulerian-Eulerian two fluid model coupled with electrostatic model and energy model. The simulated voidage profiles at different positions, bubble detachment time and initial bubble diameter are compared with experiment results from the literature. The bubble behaviors including bubble frequency and bubble numbers, combined with particle fluctuation parameters are analyzed in both charged and uncharged system. Electrostatic effect on two kinds of heat transfer coefficients are quantitatively compared, namely bubble to emulsion phase heat transfers based on the gas throughflow velocity and gas solid local heat transfer. Simulation results show that electrostatic charges decrease bubble numbers and

granular temperature, whereas the averaged heat transfer coefficients are enhanced. Overall, the electrostatic effect on the hydrodynamic and heat transfer characteristics can be revealed.

**Keywords**

Bubble behavior; Particle fluctuation; Electrostatics; Heat transfer; Fluidization

## 1. Introduction

Gas-solid fluidized beds are capable of handling huge particle volumes and thus possess exceptionally high heat transfer and mixing efficiency finding a wide range of applications including petroleum processing, environmental protection, food processing and pharmaceutical production to mention a few. Gas-solid suspensions exhibit randomness and structural instability due to the existence of bubble agitation, particle motion and gas-solid interaction resulting in a typical nonlinear transient system. From the literature reviewed, time-averaged parameters of voidage, pressure fluctuation, bubble parameters are mostly reported in the study of fluidized beds(Jung et al., 2006; Patil et al., 2005; van der Schaaf et al., 2002). In addition, these parameters can also reveal the dynamic behavior, flow structure and heat and mass transfer abilities(Acosta-Iborra et al., 2011; Patil et al., 2014; Zi et al., 2017).

However, electrostatic phenomenon is inevitable. in many industrial fluidization processes, such as ethylene polymerization, due to particle-particle and particle-wall collision and friction. The excessive accumulation of charges on the surface of the insulating particles will result in wall sheeting, particle agglomeration, or even shutdown of the plant (Sun and Yan, 2017). Moreover, electrostatic and hydrodynamic effects are interdependent. Charged particles influence bubble size and particle velocity, and ultimately performance of the equipment in relation to heat and mass transfer ability. Conversely changes in hydrodynamic properties i.e. bubble size, particle velocity and phase fraction distribution, etc., also affect the electrostatic potential distribution of the fluidized bed. Using induction probes, Chen et al. (2006) detected the

charge distribution around a rising single bubble. By comparing the predicted values from simulations and values from three theoretical models, they found that the charge density inside the bubble was zero and the particles were predominantly negatively charged in the bubble wake in comparison to the emulsion phase. Rokkam et al. (2010) introduced the electrostatic models in the CFD simulation for the first time, in which they studied entrainment of fine powder and charged particles. They pointed out that when the catalyst was negatively charged, the amount of entrainment decreased, which was in accordance with the experimental results. Hassani et al. (2013) investigated the effect of the electrostatic forces on bubble and particle motions, and inferred that when the particles were unipolar charged, the bubble size and the axial diffusion coefficient of the particles decreased. Applying CFD to study the effect of electrostatic charges on hydrodynamics, thereby predicting the heat transfer, mass transfer and fluctuation characteristics will be useful for the regulation of fluidized bed.

The bubble shape in a three-dimensional fluidized bed is difficult to characterized and pressure signal analysis is mostly applied as an intermediate way to capture the bubble size, which includes the standard deviation and incoherent analysis of pressure fluctuations. Two-dimensional fluidized bed, because of its simple structure, easy observation, is widely used in both experiment and numerical simulations. Bouillard et al. (1991) compared the experimental and simulation results for a fast bubble and calculated the pressure profile around it based on Davidson model (1963). Nieuwland et al. (1996a) then used a combination of experiments and simulations to predict bubble growth and detachment time. Different researchers have studied the effects of bubble on heat transfer (Lungu et al., 2015), electrostatics (Sun and Yan, 2016), modified computational model (Chang et al., 2016) and even scale-up effect (Knowlton et al., 2005). However, for the fluidized bed with continuous gas jet, experimental and simulation have mainly focused on phase distribution,

bubble parameters and pressure signal analysis. Studies of electrostatic effect on interphase heat transfer, local heat transfer, particle fluctuation and chaotic character of pressure signal are, as yet, rather scarce.

In this work, the gas phase fraction distribution and its fluctuation at different positions with various specific charges are studied. Simulation results are compared with the experimental data from the literature to validate the model (Kuipers et al., 1992; Nieuwland et al., 1996b). Distribution of bubble diameter along the bed height and the total number of bubbles with and without charges are calculated. The effect of electrostatic charges on the gas exchange rate, which is an important parameter used to calculate interphase heat transfer coefficient of bubbling fluidized bed as an extension of the theory from single bubble to bubbling regime is studied. Moreover, other than interphase heat transfer coefficient, the local heat transfer coefficient and particle fluctuation parameters are analyzed. Although the electrostatic effect on the time-averaged parameters and the spatial distribution of those parameters is significant, further time series analysis is required because the bed-averaged parameters may be indistinguishable due to the well mixing performance of fluidized bed. Therefore, the power spectral density, energy spectrum and chaotic analysis of the pressure signal are illuminated in this paper.

## 2. Equations of the model

The simulations of hydrodynamics at different scales, such as macroscopic scale and mesoscale scale and are mainly focused on two fluid model and discrete particle model. In the Eulerian-Eulerian approach also known as two-fluid model, each phase is considered to be completely interpenetrating with other phases with its own set of conservation and constitutive equations. Since the solid phase does not have a state equation in the continuum medium assumption of the two-fluid model (TFM), a series of closure equations are needed to describe the momentum exchange inside the particle phase, such as the radial distribution function, kinetic viscosity, bulk viscosity and frictional viscosity etc., which are important components of the kinetic theory of

granular flow (KTGF). Eulerian-Lagrangian, discrete particle model, is another commonly used method for simulating the hydrodynamic characteristics like particle motion in the fluidized bed. Although the discrete particle model can reflect the effect of particles and particles, due to its large CPU time, it's not suitable. for large size reactor. Hernández-Jiménez et al. developed a novel model and treated both the gas and the dense phase of the bed as continuum phases, whereas tracer particles were simulated as discrete entities namely fully coupled TFM-DEM simulations (Hernández-Jiménez et al., 2015). Researches have shown that the two-fluid model is in good agreement with experimental results in simulating bubble generation and motion, particle fluctuation characteristics, and particle agglomeration in dilute fluidized beds (Kumar et al., 2013; Sun et al., 2011; Zi et al., 2017). Some researchers have also compared the TFM and DPM models results for Geldart B particles (Chen and Wang, 2014; Chiesa et al., 2005). The results are in good agreement with the experimental data, therefore, two-fluid model is applied.

***TFM***

The continuity equation for the single particle dispersion system is given in Eq. (1), where $k = g$ for the gas phase and $k = s$ for the solid phase:

$$\frac{\partial}{\partial t}\left(\alpha_k \rho_k\right) + \nabla \cdot \left(\alpha_k \rho_k \mathbf{u}_k\right) = 0 \tag{1}$$

The momentum conservation equation for gas and solid phases is:

$$\frac{\partial}{\partial t}\left(\alpha_s \rho_s \mathbf{u}_s\right) + \nabla \cdot \left(\alpha_s \rho_s \mathbf{u}_s \mathbf{u}_s\right) = \nabla \cdot \overline{\overline{\tau}}_s - \alpha_s \nabla p - \nabla p_s + \beta_{gs}\left(\mathbf{u}_g - \mathbf{u}_s\right) + \alpha_s \rho_s \mathbf{g} \tag{2}$$

$$\frac{\partial}{\partial t}\left(\alpha_g \rho_g \mathbf{u}_g\right) + \nabla \cdot \left(\alpha_g \rho_g \mathbf{u}_g \mathbf{u}_g\right) = \nabla \cdot \overline{\overline{\tau}}_g - \alpha_g \nabla p - \beta_{gs}\left(\mathbf{u}_g - \mathbf{u}_s\right) + \alpha_g \rho_g \mathbf{g} \tag{3}$$

Thermal energy conservation for the solid and gas phase:

$$\frac{\partial}{\partial t}\left(\alpha_s \rho_s H_s\right) + \nabla \cdot \left(\alpha_s \rho_s \mathbf{u}_s H_s\right) = \nabla \cdot \kappa_s \nabla T_s + h_{sg}\left(T_g - T_s\right) \tag{4}$$

$$\frac{\partial}{\partial t}\left(\alpha_g \rho_g H_g\right) + \nabla \cdot \left(\alpha_g \rho_g \mathbf{u}_g H_g\right) = \nabla \cdot \kappa_g \nabla T_g - h_{sg}\left(T_g - T_s\right) \tag{5}$$

The interaction between the gas and solid phases is modeled using the parameterized Syamlal-O'Brien drag force model based on the experimental minimum fluidization velocity and the critical voidage. The momentum exchange coefficients are listed in Tab. 1 and other constitutive equations are provided in Tab. 2.

**Tab.1 Momentum exchange correlations**

| | |
|---|---|
| Syamlal–O'Brien drag function | $\beta_{gs} = \frac{3}{4}\frac{\alpha_s \alpha_l \rho_l}{v_{r,s}^2 d_s} C_D\left(\frac{Re_s}{v_{r,s}}\right)\left\|\mathbf{u}_s - \mathbf{u}_g\right\|$ |
| where | $C_D = \left(0.63 + \frac{4.8}{\sqrt{Re_s / v_{r,s}}}\right)^2$ |
| | $v_{r,s} = 0.5\left[A - 0.06Re_s + \sqrt{(0.06Re_s)^2 + 0.12Re_s(2B - A) + A^2}\right]$ |
| and | $A = \alpha_g^{4.14}$ |
| $Q = 1.28 + \frac{\log(\mathrm{P})}{\log(0.85)}$ | $B = \begin{cases} P\alpha_g^{1.28} & \alpha_g \le 0.85 \\ \alpha_g^{Q} & \alpha_g > 0.85 \end{cases}$ |

The phase stress-strain tensor $\overline{\overline{\tau}}$ in momentum conservation equation:

$$\overline{\overline{\tau}}_s = \alpha_s \mu_s \left[\nabla \mathbf{u}_s + (\nabla \mathbf{u}_s)^T\right] + \alpha_s\left(\lambda_s - \frac{2}{3}\mu_s\right)\nabla \cdot \mathbf{u}_s \overline{\overline{I}} \tag{6}$$

$$\overline{\overline{\tau}}_g = \alpha_g \mu_g \left[\nabla \mathbf{u}_g + (\nabla \mathbf{u}_g)^T\right] - \frac{2}{3}\alpha_g \mu_g (\nabla \cdot \mathbf{u}_g)\overline{\overline{I}} \tag{7}$$

Where $P_s$ is the solid pressure and is calculated using the model proposed by Lun et al. (Lun et al., 1984).

**Tab.2 Closure equations in Euler-Euler CFD simulation**

| Closure | Equation of models |
|---|---|
| Solid pressure | $p_s = \alpha_s \rho_s \left[1 + 2(1 + e_{ss})\alpha_s g_0\right]\Theta_s$ |
| Radial distribution function | $g_0 = \left[1 - (\alpha_s / \alpha_{s,\max})^{\frac{1}{3}}\right]^{-1}$ |
| Granular temperature | $\frac{3}{2}\left[\frac{\partial}{\partial t}(\alpha_s \rho_s \Theta_s) + \nabla \cdot (\alpha_s \rho_s \mathbf{u}_s \Theta_s)\right] = \left(-p_s \overline{\overline{I}} + \overline{\overline{\tau}}_s\right) : \nabla \mathbf{u}_s + \nabla \cdot (\kappa_s \nabla \Theta_s) - \gamma_s - 3\beta_{gs}\Theta_s$ |

| | |
|---|---|
| Diffusion Coefficient | $\kappa_{\Theta_s}=\frac{150\rho_s d_s\sqrt{\Theta_s\pi}}{384(1+e_{ss})g_{0,ss}}\left[1+\frac{6}{5}\alpha_s g_{0,ss}(1+e_s)\right]^2+2\rho_s\alpha_s^2 d_s(1+e_{ss})g_{0,ss}\sqrt{\frac{\Theta_s}{\pi}}$ |
| Collison dissipation | $\gamma_{\Theta_s}=\frac{12(1-e_{ss}^{\ 2})g_{0,ss}}{d_s\sqrt{\pi}}\rho_s\alpha_s^2\Theta_s^{3/2}$ |
| Collisional viscosity | $\mu_{s.col}=\frac{4}{5}\alpha_s\rho_s d_s g_0(1+e)\sqrt{\frac{\Theta_s}{\pi}}\alpha_s$ |
| Kinetic viscosity | $\mu_{s,kin}=\frac{10\rho_s d_s\sqrt{\pi\Theta_s}}{96\alpha_s(1+e)g_0}\left[1+\frac{4}{5}(1+e)g_0\alpha_s\right]^2\alpha_s$ |
| Bulk viscosity | $\lambda_s=\frac{4}{3}\alpha_s^2\rho_s d_s g_0(1+e)\sqrt{\frac{\Theta_s}{\pi}}$ |
| Frictional viscosity | $\mu_{s,fr}=\frac{p_{fr}\sin\phi}{2\sqrt{I_{2D}}}$ |
| Frictional pressure | $p_{fr}=A_s(\alpha_s-\alpha_{\min})^n$ |

In this paper, the local heat transfer coefficient is calculated using the heat transfer model applied by Patil et al. (2003) as shown in Tab. 3, where $\kappa$ is the effective thermal conductivity and is compiled in Fluent using UDF. Two groups of calculation correlations are used to obtain the relationship between Nusselt number and Reynolds number. In many simulations, such as DEM and DNS, the theory of Gunn et al. (1978) modeled well for predicting the heat transfer coefficient in a fluidized bed with a porosity of 0.35-1 and the solid phase Reynolds for turbulent regime (Lungu et al., 2015).

**Tab. 3 Thermal equations**

| | |
|---|---|
| Nusselt number correlation of Gunn | $Nu=\left(7-10\alpha_g+5\alpha_g^2\right)\left(1+0.7\,\mathrm{Re}_s^{0.2}\,\mathrm{Pr}^{1/3}\right)+\left(1.33-2.4\alpha_g+1.2\alpha_g^2\right)\mathrm{Re}_s^{0.7}\,\mathrm{Pr}^{1/3}$ |
| Solid Phase thermal conductivities | $\kappa_s=\frac{\left(\beta A-(1-\beta)K\right)\kappa_{g,o}}{\sqrt{1-\alpha_s}}$ |
| Gas Phase thermal conductivities | $\kappa_g=\frac{\left(1-\sqrt{1-\alpha_g}\right)\kappa_{g,o}}{\alpha_g}$ |
| $K=\frac{2}{1-\frac{B}{A}}\left[\frac{A-1}{\left(1-\frac{B}{A}\right)^2}\frac{B}{A}\ln\frac{A}{B}-\frac{B-1}{1-\frac{B}{A}}-0.5(B+1)\right]$ | $A=\frac{\kappa_{s,o}}{\kappa_{g,o}}\quad B=1.25\left(\frac{1-\alpha_g}{\alpha_g}\right)^{10/9}\quad\beta=7.26\times10^{-3}$ |

In recent years, many researchers have proposed different electrostatic models in fluidized bed (Jalalinejad et al., 2012; Kolehmainen et al., 2016, 2017; Rokkam et al., 2010). The electrostatic static model

proposed by Rokkam et al. can be applied to characterize the bubbles motion, particle entrainment and electrostatic potential distribution of the multi-particle dispersion system, which is consistent with experiment work reported by Wang et al. (2008). They measured the axial and radial distributions of the electrostatic potential in the polyethylene fluidized bed using an electrostatic impact probe, and obtained the electrostatic potential distribution of the entire fluidized bed, which proved that the lower part of the PE fluidized bed was mainly negatively charged.

The governing equations for the simulation are based on the Maxwell equations and the Faraday's law, as shown in Tab. 3. The relative permittivity of the gas phase (air) and the solid phase (glass beads) are 1 and 7.6 respectively. The relative permittivity of the gas solid mixture can be obtained by curve fitting according to $\alpha_g = \left(\frac{\in_s - \in_m}{\in_s - \in_g}\right)\left(\frac{\in_g}{\in_m}\right)^{1/3}$ (Rokkam et al., 2010). Steps for embedding a user defined scalar into a Fluent are described in detail the work of Rokkam et al, hence, here will not be discussed.

**Tab. 3 Electrostatic model**

| | |
|---|---|
| Faraday's law | $\nabla \times E = 0$ |
| Electric force | $F_e = QE$ |
| Electric potential | $E = -\nabla\varphi$ |
| Gauss's law | $\nabla \cdot D = q_v$ |
| Electric displacement | $D = \in_0 E + P$ |
| Induced polarization | $P = \in_0 \chi_e E$ |
| Relative permittivity | $\in_m = 1 + \chi_e$ |
| | $\in_m = 7.62 - 12.0\alpha_g + 5.64\alpha_g^2$ |
| Poisson equation | $\nabla \cdot \left(\alpha_g\left(5.64\alpha_g - 12.0 + \frac{7.62}{\alpha_g}\right)\nabla\varphi\right) = -\frac{q_v}{\in_0}$ |

***Boundary conditions***

In this paper, the experiment configuration of the fluidized bed with a central orifice in the work of Kuipers et al. is used in the two-dimensional simulation (1992). Previous studies have shown potential and accuracy for the two dimensional simulation for both pseudo 2D and 3D simulation by considering proper wall friction models (Lungu et al., 2016; Sun and Yan, 2016). Thus, for simplify, two dimensional simulations are applied. The geometrical parameters and physical properties of the simulation system are shown in the Tab. 4. The fluidized bed is meshed with a structured grid, using a horizontal grid size of 0.0075 m and a vertical grid size of 0.01 m. The velocity, momentum and UDS are solved by the second order upwind scheme. The volume fraction is solved by the Quick scheme. Phase Coupled SIMPLE is adopted for the pressure-velocity coupling. The time step is 0.0001 s.

The gas phase boundary condition is non-slip, and the particle phase is the partial slip condition proposed by Johnson and Jackson (2006), where the spectacular coefficient is 0.5 and particle wall restitution coefficient.

**Tab. 4 Structural scheme and physical parameter**

| Physical parameters | Values | Physical parameters | Values |
|---|---|---|---|
| Bed width (m) | 0.57 | Gas phase density (kg $m^{-3}$) | 1.2 |
| Bed height (m) | 1 | Gas phase viscosity (Pa s) | $1.85\times10^{-5}$ |
| Jet orifice width (m) | 0.015 | Solid phase density (kg $m^{-3}$) | 2550 |
| Initial bed level (m) | 0.5 | Solid diameter (μm) | 500 |
| Jet velocity (m $s^{-1}$) | 10 | Voidage at Minimum fluidization | 0.402 |
| Specific Charge (μC $kg^{-1}$) | -0.4, -0.8 | Minimum fluidization velocity (m $s^{-1}$) | 0.25 |
| Operating temperature (K) | 288.16 | Operating pressure (Pa) | $1.013\times10^{5}$ |

## 3. Results and discussion

### 3.1 Bubble dynamics

3.1.1 Voidage profile

Gas phase fraction or voidage affects the interaction between gas and solid phase in the fluidized bed and its distribution can also reflect the various hydrodynamic characteristics, such as particle motion, bubble generation, coalescence and local transfer. Fig. 1 shows the comparison of the experiment results by Kuipers et al. (1992) and predicted voidage profiles along the bed height at different positions from the central axis. The experiment was carried out in a two dimensional fluidized bed with a central jet and the experiment condition was the same as the simulation set-up in Tab. 4. The time-averaged voidage in the simulation averaged over 30 s and the experiment computed for a time span of 60 s are in good agreement. When the electrostatic charge is not taken into account, the voidage is large at 0.375 cm from the central axis due to the bubble formation in vicinity of jet region, as depicted in Fig1 (a). During the bubble rising period, there are already solid particles falling into the inside the bubble, thus, the voidage decreases with the bed height. Moreover, the bubble will drift away from center line to a certain extent due to the anisotropic nature of hydrodynamics within fluidized bed.

At the distance of 9.375 cm from the center, Fig.1 (b), voidage increases with the bed height because particles are squeezed from the center line during bubble formation and rising. Moreover, bubble volume expansion and dispersion within the fluidized bed will also influence the voidage profile here. Fig1. (c) illustrates voidage distribution near the wall, it can be seen that in the region below 0.14 m, the voidage is close to the minimum voidage, which shows that particles motion and mixing are weak and a dead zone exists.

When the particles are charged, it can be seen from Fig. (a), when $q_m$ = -0.8 μC/kg, the voidage below $y$=0.31 m significantly decreases. Here, due to the impact of high-speed jet air, bubble interaction in the

vertical direction is strong, and solids in the particle vortex are more likely to entrain and accumulate, so the solid phase concentrate near the central axis increases. As can be seen from Fig.1 (b), the voidage increases at 9.375 cm from the central axis after the particles are charged compared to the uncharged condition. The particles in this region where strong bubble interaction happens, move towards the wall, and the repulsive force between the same charge particles in the transition region increases the voidage. Fig.1 (c) shows that with the same charge, dead zone near the wall increases. From the force analysis around the bubble boundary by , the electrostatic forces acting on the left and right sides of the bubbles are directed toward the wall, which tends to gather the particles on the wall, resulting in a decrease of the voidage (Jalalinejad et al., 2012).

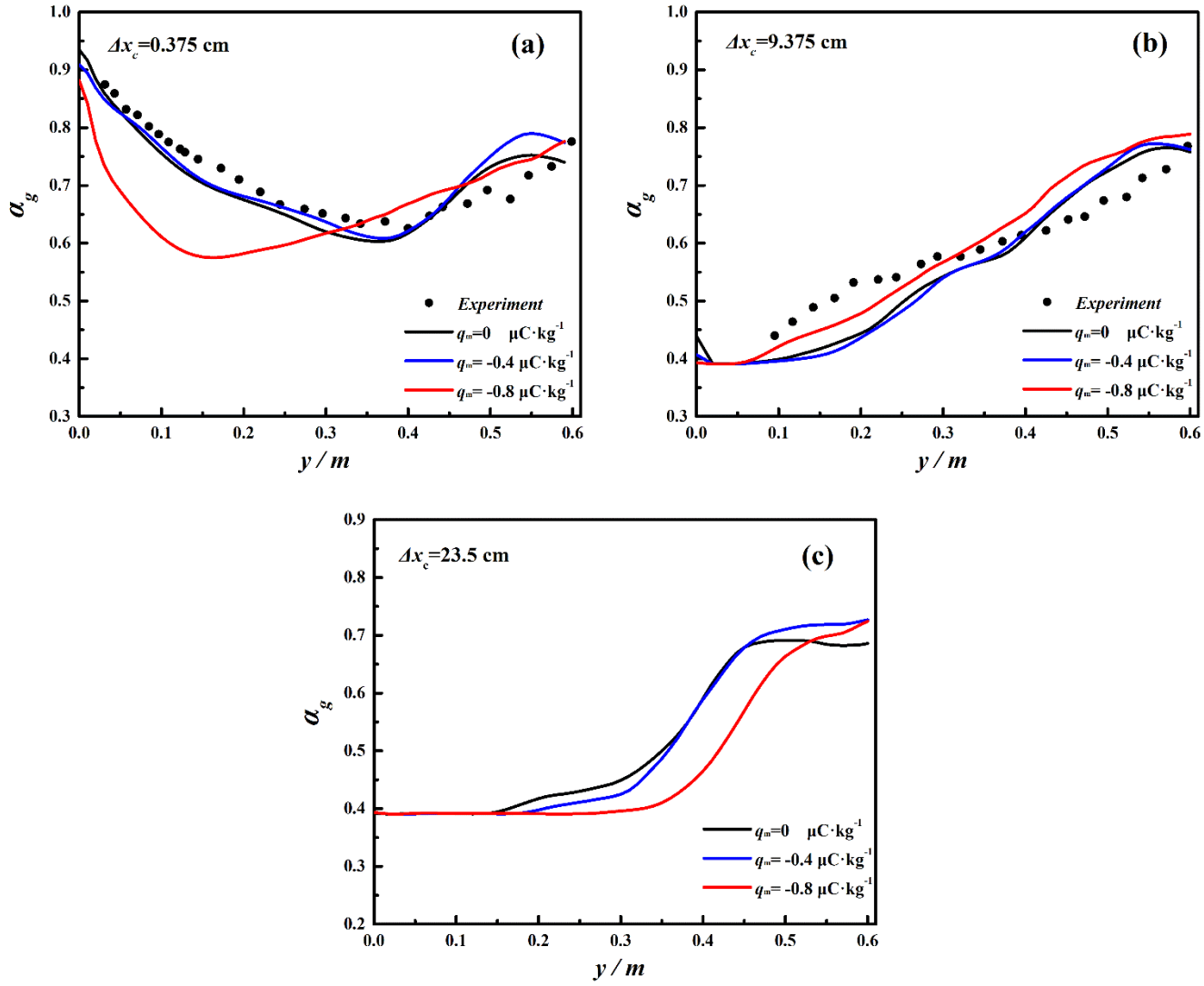


**Fig.1 Averaged voidage profile from (a) 0.375 cm (b) 9.375 cm (c) 23.5 cm of the central axis line along the bed height**

3.1.2 Bubble frequency

The hydrodynamics in the fluidized bed is are connected to the bubble behaviors. The bubble dispersion, bubble diameter and velocity affect the heat transfer and mass transfer in the reactor. The prediction of the initial bubble diameter and bubble frequency at the orifice plays an important role in the study of the subsequent hydrodynamic behavior. Bubble frequency reflects the number of bubbles appearing in a bed during a certain time period, that is $f_b = N_b / t_s$, and is closely related to the gas and particles motion. Fig. 2 shows the porosity fluctuation at 3.13 cm above the orifice, and a peak larger than 0.85 represents the generated bubble. Fig.2 (a) shows the voidage fluctuation when the particles are not charged. The bubble frequency is 5.6 Hz, which agrees well with the experimental result of 6 Hz in Fig. 2 (d). The bubble frequency of the 2D structure can be predicted according to the Davidson-Schüler model (Kuipers et al., 1991):

$$f_b = \left[ \left( \frac{16 C_0^2}{\pi} \right) \left( \frac{u_0 d_0}{g^2} \right) \right]^{1/3} \tag{8}$$

When $C_0$ is taken as 1, bubble frequency is 5.01 Hz. Fig.2 (b) and Fig.2 (c) represent the voidage fluctuation at the same position where the particle specific charge is -0.4 μC/kg and -0.8 μC/kg respectively, corresponding to the bubble frequency of 5.26 Hz and 3.85 Hz respectively. As shown in Fig. 2 (b), when $q_m$=-0.4 μC/kg, the peak shape becomes sharper, the platform of more than 0.85 becomes wider and the peaks less than 0.85 increase. When $q_m$=-0.8 μC/kg, the bubble frequency is obviously reduced indicating that the generated bubbles are more easily detached from the orifice with a low gas fraction and will cause the initial bubble diameter to decrease.

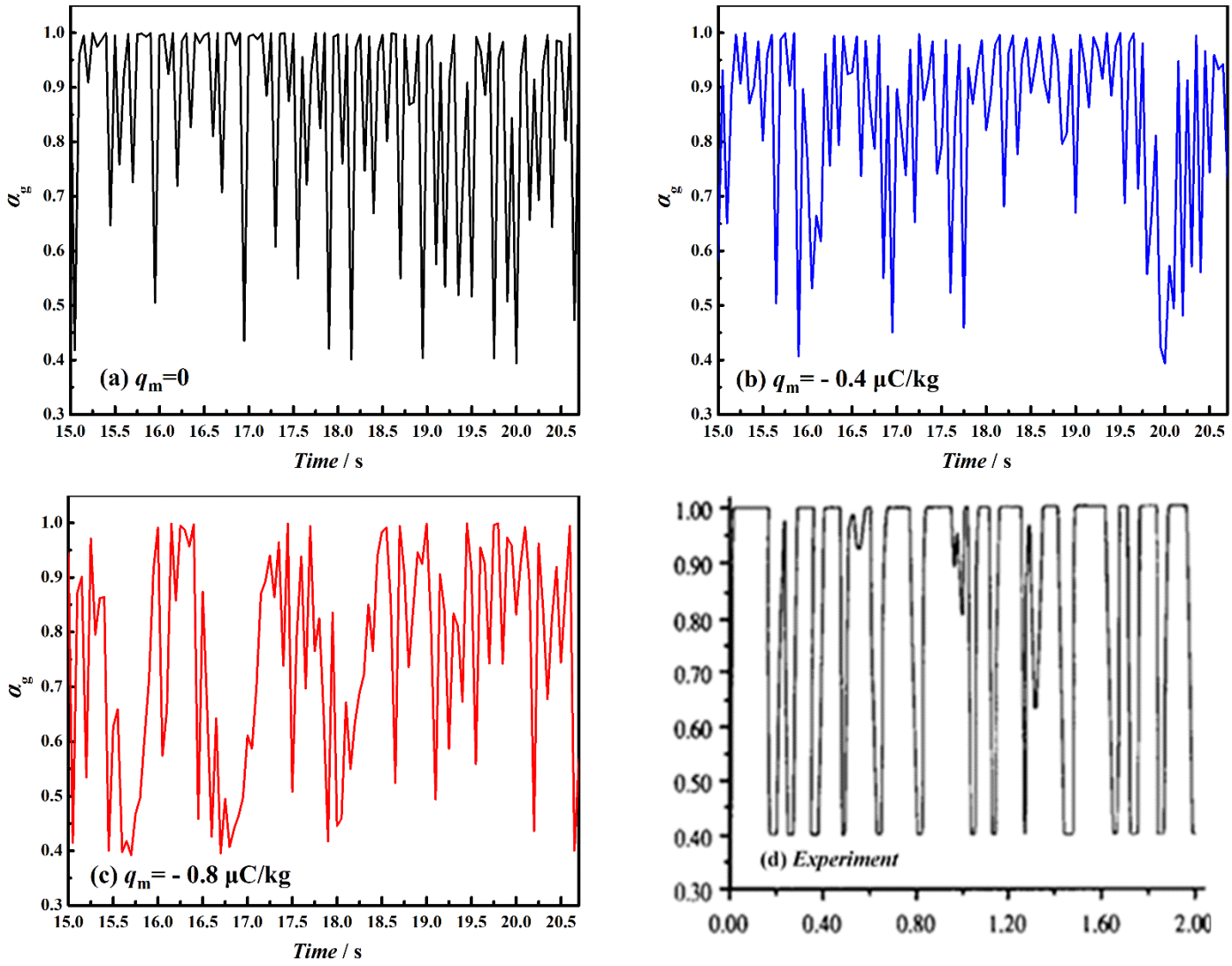


**Fig.2 The voidage varies with time at 3.13 cm from orifice on the central axis where (d) is the experiment result of Kuipers (1992) et al.**

3.1.3 Bubble diameter

In this section, the effect of electrostatic charges on the bubble growth, breakup and coalescence of the bubbles in the bed, as well as the effect of the charge on the bubble diameter distribution and the bubble size are studied in detail. It is important to emphasize that during the experiment, the fluidization velocity, the fluidization time both affect the charge to mass ratio of the particles (Chalermsinsuwan et al., 2014; Yang, 2003). Without changing the fluidization conditions, the charge of the particles in the bed is difficult to control, and the experimental research on the effect of electrostatic on hydrodynamics is difficult. In the simulation,

different charges were loaded into the fluidized bed with the same jet velocity by UDF, and the influence of the charge-to-mass ratio on the bubble behavior was studied.

Fig.3 shows the bubble contours with different charge-to-mass ratio at the same time (20.35 s-20.26 s) under the same jet velocity. From Fig. 3 (a) - (d), when the particles are not charged, the bubbles are elongated in shape when they are generated from the distribution plate, and the averaged bubble diameter of the first bubbles detached from the orifice is 0.123 m. Since the porosity of the injection area increases and the bubbles are more easily separated from the distribution plate after a period of fluidization, the averaged diameter of the first bubbles detached from the orifice within 30 s of this paper is less than 0.17 m of the single bubble experiment of Kuipers et al (1991). But the initial bubble diameter of this paper is 0.175 m, which is in good agreement with the experiment result. The upward movement of the bubble, due to the subsequent air flow and the strong interaction between the bubbles, is depressed at the bottom and the aspect ratio increases. When the bubbles reach the surface of the bed, they are flattened, where the bubble coalescence and breakage are strong. Near the left side of the wall, $y$ = 0.2-0.25 m, the bubble velocity is very small, and the coalescence and breakage basically do not occur. Fig. 3 (e) - (h) illustrate the bubble contours with charge-to-mass ratio of -0.4 μC / kg. It can be seen from the Fig.3 that the generated bubbles are more elongated. And the averaged diameter of the first bubbles detached from the orifice is 0.108 m. The size of the bubbles near the wall at $y$ = 0.17-0.5 m becomes smaller and the bubbles become more dispersed. Moreover, the voidage in the vicinity of the bed level surface is increased, and the bubbles are more easily broken. When the charge-to-mass ratio is -0.8 μC / kg, it can be seen from Fig. 3 (i) - (l) that the particle phase fraction in the generated bubbles is obviously increased. Hassani et al. simulated the bubbling fluidized bed with the same positive charged particles by DEM and the simulation results also showed that the boundary of the bubble became very blurred with the increase of the positive charges (Hassani et al., 2013). The bubble is stretched in the axial direction,

but the average initial bubble diameter is only 0.089 m according to the definition of the bubble boundary. As can be seen from Fig. 2 (c), larger specific charge increases the particle fraction near the wall, and the number of bubbles near the wall are reduced. When the bubble moves to the top of the bed level, it can be seen that the elongation of the bubbles becomes more pronounced.

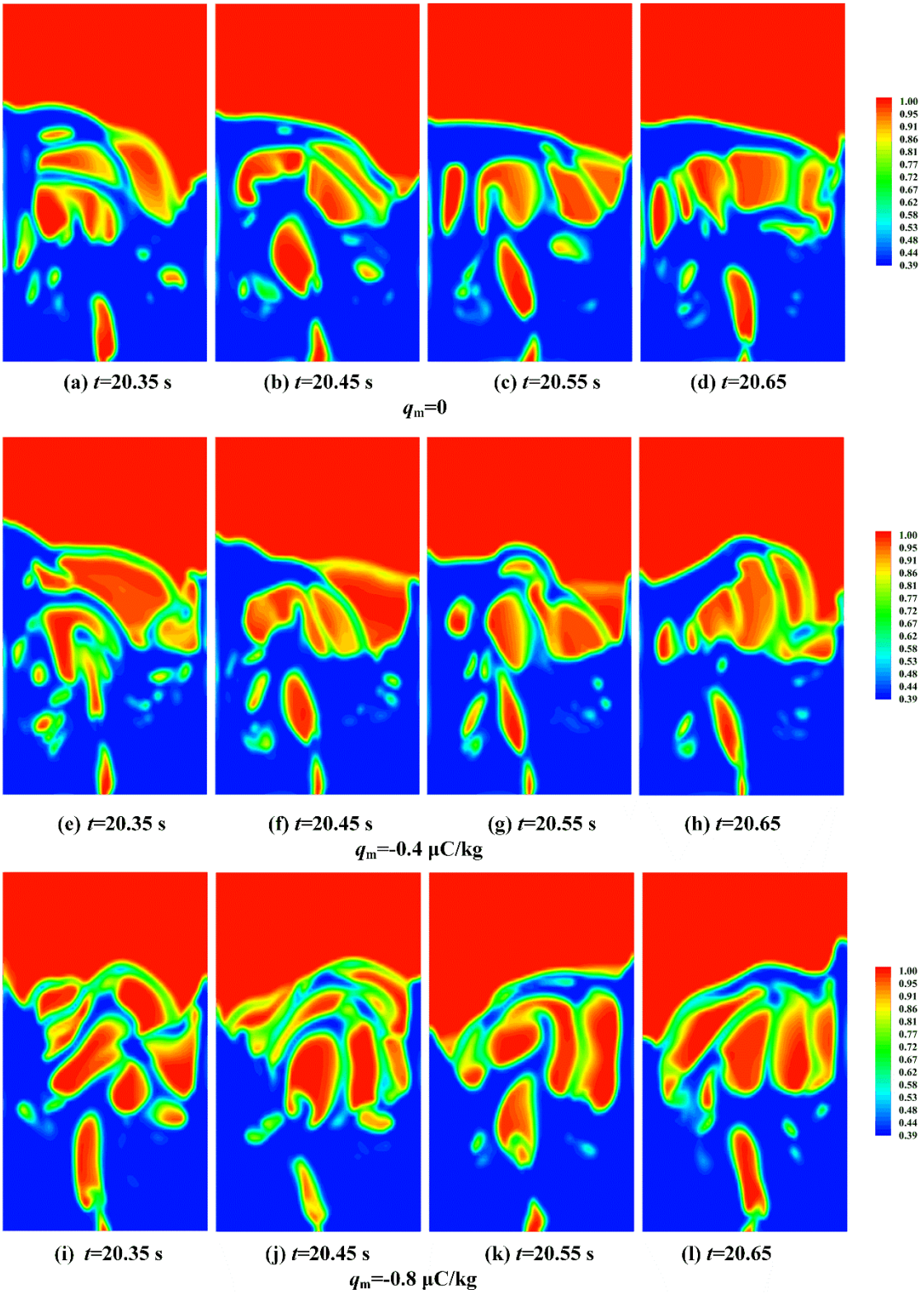


(a) $t$=20.35 s (b) $t$=20.45 s (c) $t$=20.55 s (d) $t$=20.65

$q_m$=0

(e) $t$=20.35 s (f) $t$=20.45 s (g) $t$=20.55 s (h) $t$=20.65

$q_m$=-0.4 μC/kg

(i) $t$=20.35 s (j) $t$=20.45 s (k) $t$=20.55 s (l) $t$=20.65

$q_m$=-0.8 μC/kg

**Fig. 3 Bubble contour snapshot with charge-to-mass ratio of $q_m$= 0, -0.4, -0.8 μC/kg at the same time (20.35 s-20.26 s) under the jet velocity of 10 m/s**

Fig. 4 depicts the mean equivalent bubble diameter varies with height in 15-25 s under different specific charges. Jalalinejad et al. (2012) simulated the bubbling fluidized bed with a charge-to-mass ratio of -0.36 μC / kg and particle density of 2500 kg / m$^3$. Their results indicated that, at 1.5 $U_{mf}$ and 2.5 $U_{mf}$, the bubble with charge was smaller than the bubble diameter without charge, and the introduction of electrostatic charges caused the bubble diameter at 2.5 $U_{mf}$ to be slightly higher than the bubble diameter without charges at the proximity of the bed level. At the same time, under this simulated condition, the number of bubbles decreased by 33% and 0.25%, respectively. It can be seen from Fig. 3 and Fig. 4 that when the specific charge is -0.4 μC / kg, the average bubble diameter is smaller than that in the uncharged system in the range of $y$ <0.2 m, 0.29 m <$y$ <0.5 m and $y$> 0.57 m.

When the specific charge increases to -0.8 μC / kg, the initial bubble diameter in the region below $y$ = 0.14 m is still smaller than the bubble diameter without charges, but at 0.14 m <y <0.6 m, The average bubble diameter and the growth rate of the bubble are larger than those of the bubbles in uncharged system, which may be due to the electrostatic effect on the bubble elongation, and the bubble elongation will increase gas through flow (Gera and Gautam, 1994; Yusuf et al., 2012). On the other hand, when the particles are not charged or charge is small, it can be seen from the above Fig. that there are still some small bubbles near the wall, which results in slightly smaller average diameter in the middle of the bed. In the vicinity of the bed level of 0.55 m, the bubble diameters in the three charged conditions are larger than that of the bubbles when no charge is added. However, when the height is more than 0.6 m, the bubble diameters are smaller than that without charges.

However, the effect of electrostatics on the bubble diameter in the gas-solid fluidized bed is complicated. Yao et al. adjusted the air humidity to control the charge dissipation rate in the gas-solid fluidized bed and obtained the standard deviation of pressure at different charge-to-mass ratios(Yao et al., 2002). The experimental results showed that the

standard deviation decreased with the air humidity, that is, the size of the bubble decreased with the decreasing charge-to-mass ratio. Comparing the simulation results in the present work, it can be seen that between -0.4 μC / kg and -0.8 μC / kg, electrostatic charges can significantly change the bubble characteristics and hydrodynamic characteristics. While the $q_m$= -0.4 μC / kg and below, the influence of the specific charges on the hydrodynamics is not obvious.

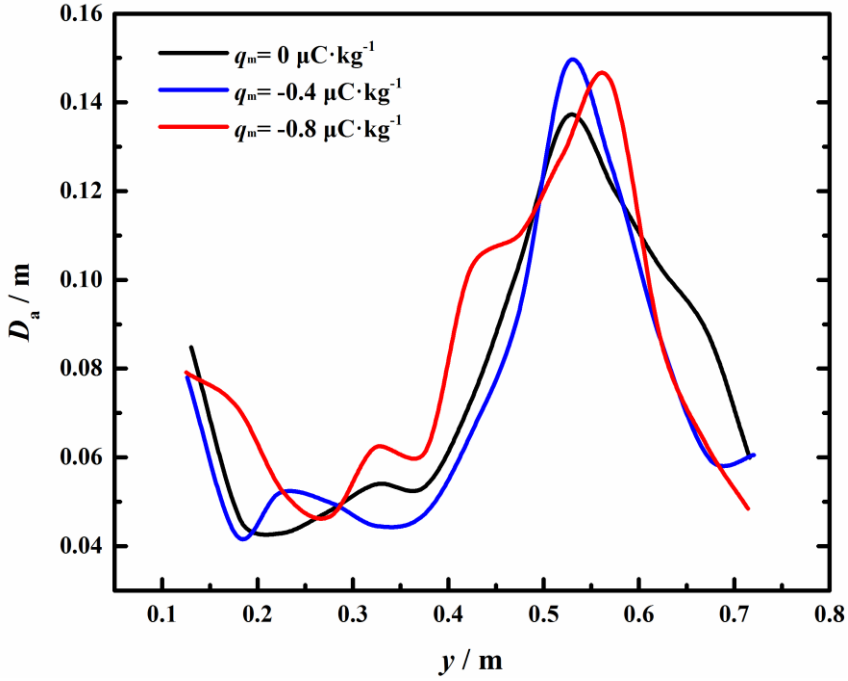


**Fig.4 Average bubble diameters along with the bed height within 10 s**

To explain the electrostatic effect on the average bubble diameters, Fig. 5 shows the number of bubble diameters for different specific charges. Compared to the simulation results of Jalalinejad et al. (2012), which showed that the number of bubbles was reduced by 33% and 0.25% respectively at 1.5 $U_{mf}$ and 2.5 $U_{mf}$ . The number of bubbles without charges in 10 seconds is 1013, and when the specific charge is -0.4μC / kg and -0.8 μC / kg, the number decreases by 3.6% and 23% respectively in the current study. Dong et al. also measured the dynamic bed level of the PP fluidized bed by experiment. It was found that the fluctuation of bed level was significantly increased when the particles were not charged, and the average porosity of the bed was increased by 6% compared with the saturated charged particles, indicating that electrostatic effect made the bubble volume fraction reduce(Dong et al., 2015a). This phenomenon is in accordance with the external electric field on bubbles, which would make diameters of a single bubble and bubble

diameters in fluidized bed decrease and the number of bubbles reduce (Kleijn van Willigen et al., 2005; Sun et al., 2015). It can be seen from Fig.5, when the particles are charged, the probability of emergence of large-size bubbles increases.

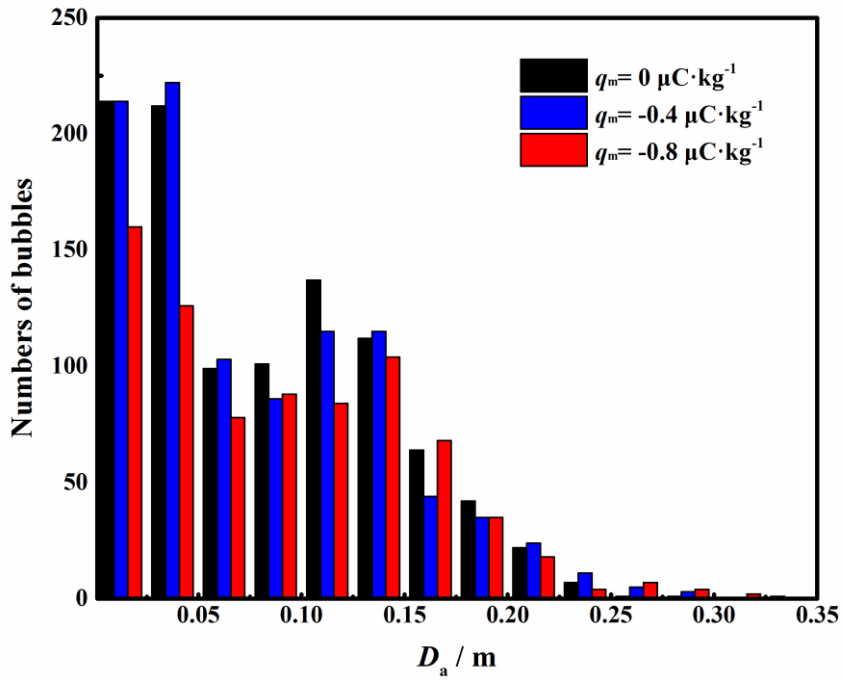


**Fig. 5 Bubble size distribution of different charges**

### 3.2 Particle fluctuation characteristics

#### 3.2.1 Particle velocity

As described above, the increase in specific charge causes the bubble phase fraction to decrease and the number of bubbles to decrease. Because the coalescence, rising and breakage of the bubbles in the fluidized bed are the driving force for particle movement, thus changes in the bubble behavior caused by electrostatic charges will inevitably lead to changes in the movement of particles. This section therefore examines the effects of electrostatics on bubble motion and fluidized particle motion.

Fig.6 shows the variation of particle velocities in the time period 15 - 25 s at different heights in the fluidized bed with different specific charges. Fig.6 (a) and 6 (b) display the particle velocities in the *x*-direction and the *y*-direction at $x$ = 0.1 m, $y$ = 0.1, Fig. 6 (c) and 6 (d) are the particle velocities in the *x*-direction and the *y*-direction at $x$ = 0.1 m, $y$ = 0.5 and dashed lines indicate the average values under each simulated condition. From Fig. 6 (a), the mean particle

velocity at the bottom of the bed in the $x$ direction is 0.636 m / s when the particles are not charged. When the charge-to-mass ratio increases from -0.4 μC / kg to -0.8 μC / kg, the average particle velocity is 0.629 m / s and 0.243 m / s respectively, and the particle fluctuation strength decreases obviously as in Fig. 6(a). In the bottom of the bed, when the particles are not charged, the average particle velocities in the $y$-direction are -0.528 m / s, -0.481 m / s and -0.249 m / s, respectively as in Fig. 6(b) with $q_m$=0, -0.4, -0.8 μC / kg. With the increase of the specific charges, the number of bubbles in the lower part of the bed near the wall decreases, and the turbulence of the particles decreases. It can be seen that the electrostatic charge is not conducive to the particles mixing at the bottom of the bed and near the wall, thus particles are also prone to accumulation.

From Fig. 6 (c) and 6 (d), it can be seen that at the position closed to the bed level ($x$ = 0.1 m, $y$ = 0.5 m), the average velocity in the $x$ direction increases, and the mean particle velocities with $q_m$=0, -0.4 and -0.8 μC / kg in the $x$ direction are -0.547 m / s, -0.581 m / s and -0.822 m / s, respectively, indicating that the particles are more likely to move toward the wall and enrich. As in Fig. 6 (d), the particles velocity fluctuates between -1.5 and 2 m / s, and the particle movement is more complicated. The mean particle velocities in the $y$ direction are 0.263 m / s, 0.309 m / s and -0.1 m / s respectively, with $q_m$=0, -0.4 and -0.8 μC / kg.

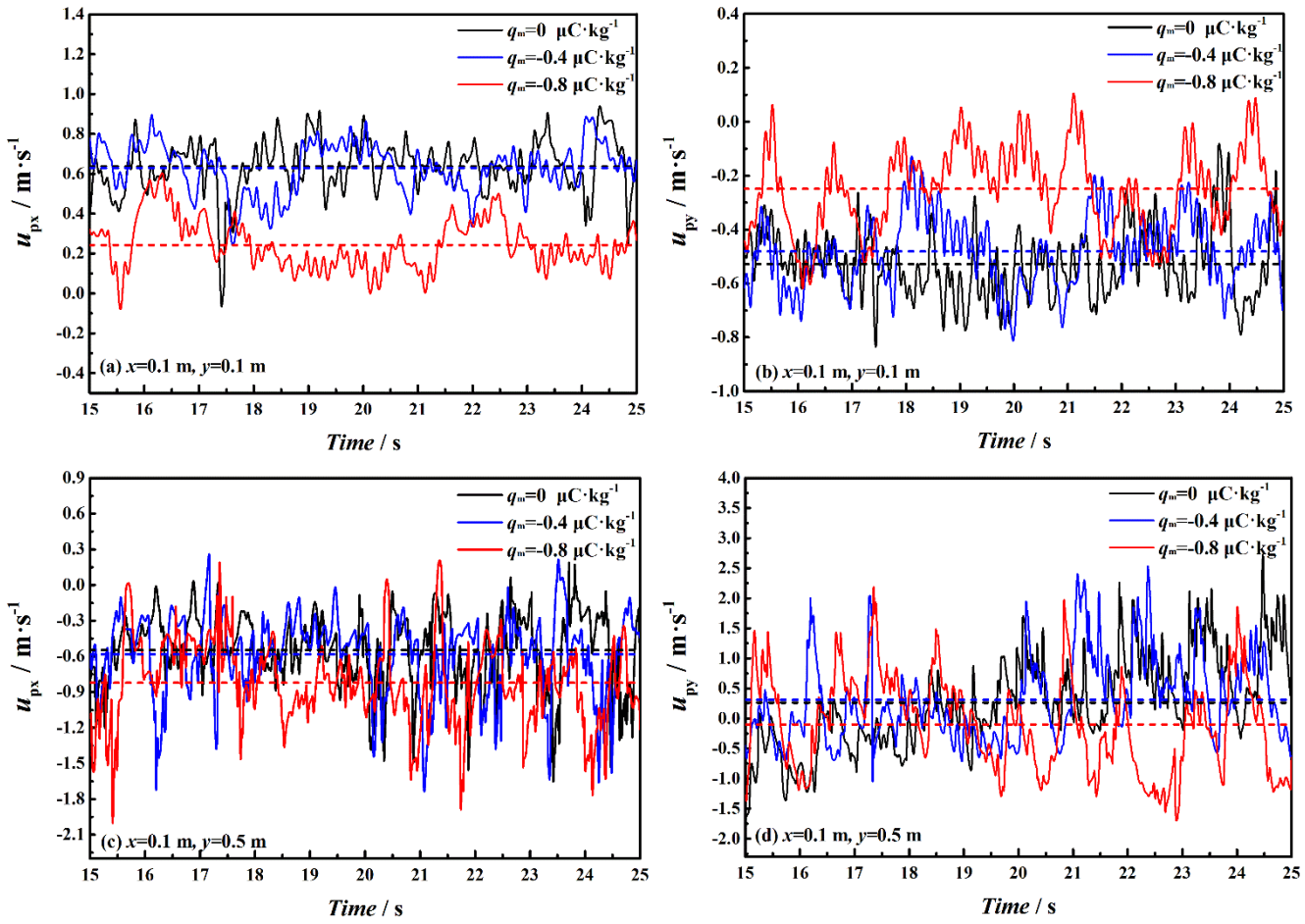


**Fig. 6 Particle fluctuation velocity (a) in *x*-direction at *x*=0.1 m, *y*=0.1 m (b) in *y*-direction at *x*=0.1 m, *y*=0.1 m (c) in *x*-direction at *x*=0.1 m, *y*=0.5 m (d) in *y*-direction at *x*=0.1 m, *y*=0.5 m where the dashed lines are average with different specific charge.**

When the specific charge is small, the hydrodynamics and particle circulation characteristics within the bed do not change significantly. But when the specific charge is large, the average particle velocity changes obviously, which includes the change of the average velocity in the direction of the *y*-direction at the bed level. It can be deduced that when the particles are negatively charged, the particles are more likely to move downwards and decrease the elutriation. This phenomenon can be explained that the experiment presented by Dong et al. (Dong et al., 2015b) and studied the electrostatic effect on the collision energy distribution in the axial direction for PP particles at different operating air velocities. The results also showed that particle fluctuation and collision energy were significantly weakened, in the charged system,

3.2.2 Granular temperature

The granular temperature represents the collision and random motion intensity at the particle scale, and is related to the normal stress, which is an important parameter to characterize the particle movement. Moreover, granular temperature is a steady state parameter determined by the cohesive force and inertial force applied by the local gas environment and the granular environment on the particles, characterizing the hydrodynamic characteristics of the multiphase flow field (Cody et al., 1996). In 2D simulation, the granular temperature is defined as follows:

$$\theta_{\text{laminar}} = \frac{1}{3}\left[\left\langle C_y C_y \right\rangle + 2\left\langle C_x C_x \right\rangle\right] \tag{9}$$

Where the particle normal stress is calculated by the instantaneous fluctuation velocity in the axial and radial directions, i.e. the difference between the instantaneous velocity and hydrodynamic velocity:

$$\left\langle C_i C_i \right\rangle = \frac{1}{n_p}\sum_{k=1}^{n_p}\left(c_{ik}(x,t) - u_i(x,t)\right)\left(c_{ik}(x,t) - u_i(x,t)\right) \tag{10}$$

$$u_i(x,t) = \frac{1}{n_p}\sum_{k=1}^{n_p} c_{ik}(x,t) \tag{11}$$

Fig. 7 shows the variation of average laminar granular temperature along radial direction. It can be seen from Fig. 7 that when the particles are not charged, the granular temperature is greatly increased at the jet region ($y$ = 0.025 m) due to the strong particle motion and collision caused by the high velocity jet flow. However, as the bubbles begin to generate, the particles are squeezed to both sides of the nozzle, the turbulence of the particles decreases and the granular temperature decreases. When the bubble is detached from the orifice, the particle volume fraction decreases, resulting in the increasing space of particle movement and the increase of granular temperature.

Under the influence flow structure such as particle vortex, eddy and particle agglomerate, the particle temperature begins to decrease, and then the bubble begins to break up, resulting in the increase of the average free path of the particles and the increase of the granular temperature near $y$ = 0.515 m. When the $q_{\text{m}}$ = -0.4

μC / kg, the peak value reduces and the changes are not obvious below $y$=0.4 m. When $q_m$ = -0.8 μC / kg, the average granular temperature further decreases, indicating that the electrostatic effect limits the fluctuation ability of single particle.

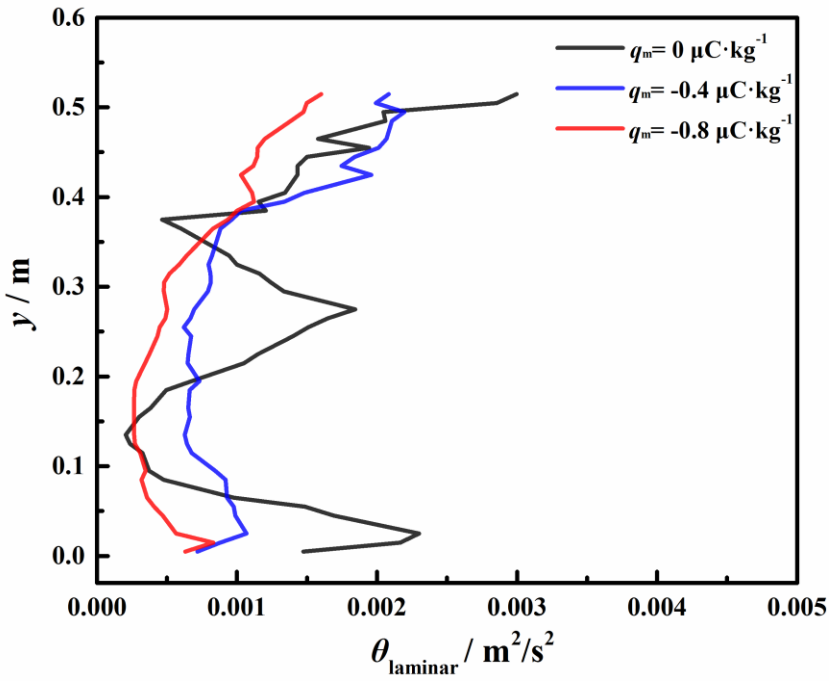


**Fig. 7 Comparison of average laminar granular temperature along the axial direction**

### 3.3 Gas interchange

In the previous section, the phase holdup and particle fluctuation parameters have been calculated to reflect the bubble characteristics and particle motion in the fluidized bed, and these parameters will also affect the gas exchange from bubble phase to emulsion phase. The amount of gas exchange between the emulsion phase and the bubble phase not only affects the bubble diameter distribution in the fluidized bed, but also affects the chemical reaction and heat transfer. The heat transfer model proposed by Davidson and Harrison (Davidson and Harrison, 1963) consists of two parts, the flow heat transfer and convective heat transfer:

$$H_{be,\mathrm{DH}} = \frac{V_{\mathrm{be,DH}}\rho_g C_{pg} + h_{bc}S_{bc}}{V_b} \tag{12}$$

Where $V_{be}$ denotes the gas volume flowrate from bubble to bubble cloud, which in Davidson model, defines as $V_{be,DH}=q_{DH}L=2u_{mf}DL$, where $L$ is the thickness of the fluidized bed and $q$ is the gas interchange. Thus, for a cylindrical bubble, the heat transfer coefficient containing conduction term and convection term is:

$$H_{be,DH}=\frac{2}{\pi}U_{mf}\rho_f C_{pg}+0.6\frac{\left(k_g\rho_g C_{pg}\right)^{0.5}g^{0.25}}{D^{0.25}} \tag{13}$$

For the heat transfer of single bubbles, the simulation results are in good agreement with the experimental values and the calculated values of the Davidson model(Patil et al., 2014). However, there are strong interactions between the bubbles in the bubbling bed with central jet, and the factors such as particle vorticity and electrostatic effect will change the througflow coefficient, affecting the heat transfer within the fluidized bed. Hernández (Hernandez-Jimenez et al., 2013) calculated the gas exchange coefficient and the cross-flow ratio in the bubbling fluidized bed using the corrected velocity, where $U$ / $U_{mf}$ had a maximum of 2.75, where $U_{th}$ is the throughflow velocity:

$$U^*=U_{mf}+U_{th} \tag{14}$$

According to the theory of Valenzuela and Glicksman, the gas in the bubbling fluidized bed could be divided into three parts: the gas in the dense phase, the gas throughflow and the gas in the bubble, where the throughflow was related to the geometry of the bubble (Valenzuela and Glicksman, 1985). Thus, the average superficial gas velocity is the composition of dense phase velocity, throughflow velocity and visible bubble flow. The last two components are independent of bubble motion and therefore, gas flow in excess of the visible bubble flow in the bubbling fluidized bed could be expressed as Equation (15), where the geometric factor $M$ can be solved by Equation (16).

$$U^*=U_{mf}+\frac{1}{1-M}U_d \tag{15}$$

$$M=\begin{cases}\dfrac{\left(\rho-\sin 2\rho/2\right)\cos\rho}{\sin^3\rho} & where\ \cos\rho=a/b, a<b\\ \dfrac{1}{\sin^2\phi}-\dfrac{\cos^2\phi}{2\sin^3\phi}\ln\left(\dfrac{1+\sin\phi}{1-\sin\phi}\right) & where\ \cos\phi=b/a, a>b\end{cases} \tag{16}$$

The throughflow velocity $U_{th}$ calculated by without electrostatic charges is 1.40 m / s and the correction speed $U^*$ is 1.65 m / s. When $q_m$=-0.8 μC/kg, the throughflow velocity $U_{th}$ is 1.45 m/s and the correction speed $U^*$ is 1.70 m / s. For clarity, the interchange volumetric gas flow is also calculated to compare the result by Equation (15). The gas volume flowrate between the bubble phase and emulsion phase is calculated based on the bubble centroid velocity and gas velocity at the bubble boundary, where the area with $\alpha_g \geq 0.85$ is defined as the bubble:

$$q_{be} = \int_{\Omega_b} \alpha_g \left[ -\left(u_{gh} - u_{bh}\right) dy + \left(u_{gv} - u_{bv}\right) dx \right] \tag{17}$$

Fig. 8 is a statistical relationship between the gas interchange and bubble diameter according to the definition above, through averaging the gas interchange in different diameters range, where the number of bubbles calculated is more than 100. The slopes of the two fitted lines in Fig.8(a) and Fig(b) are 3.17 and 3.29, respectively. By the definition of gas interchange, the corrected form is as follows:

$$q_{be} = 2U^*_{cal} D_a \tag{18}$$

Where $U^*_{cal}$ is the predicted gas flow considering gas to emulsion phase interchange. Thus, $U^*_{cal}$ from the slope of fitted lines are 1.59 and 1.64 for $q_m$=0 and -0.8 μC/kg. After the particles were charged, the bubbles were stretched in the axial direction, and bubble rise velocity increased slightly. At this time, the throughflow velocity increased. Through comparing of the fitted value $U^*_{cal}$ and the theoretical value $U^*$, the relative deviation is 4% and 3% respectively in the uncharged system and charged system and the interphase heat transfer coefficient in these two systems are 1256.46 W / $m^2$K and 1294.39 W / $m^2$K.

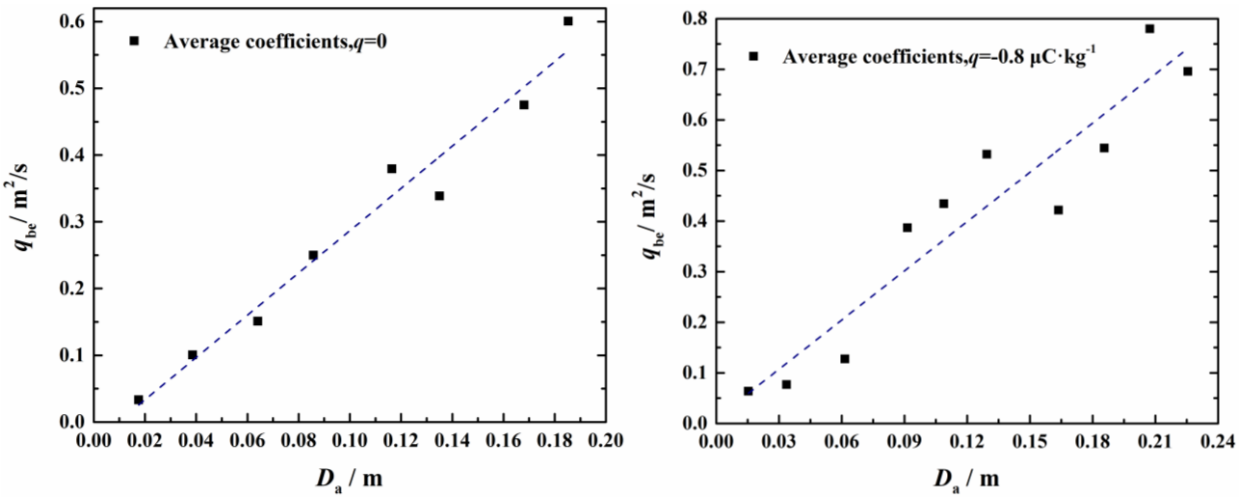


**Fig. 8 Gas interchange against bubble diameter by statistic calculation**

Through the calculation of the relationship between gas interchange and bubble diameter, the larger the bubble diameter, the greater the gas interchange. However, from Fig. 8, the effects of electrostatics on the bubbles are various at different heights. The electrostatic charges effect the diameter of the primarily generated bubbles and the bubbles near the bed level. Therefore, the bed geometry, bed level and bubble sizes are all considered to affect the gas interchange. Although the throughflow velocity slightly decreases in the uncharged system, the overall averaged diameters in the fluidized bed within 10s, due to different breakage and coalescence strength, are not necessarily proportional to the gas interchange. In this situation, the overall averaged bubble diameters are 7.8 cm and 8.1 cm, respectively, for $q_m$=0 and -0.8 μC/kg.

### 3.4 Local heat transfer coefficient

Heat transfer between the particles and gas in the gas-solid fluidized bed is another important heat transfer mechanism. Fig.9 shows the effect of electrostatics on the local heat transfer coefficient, where the ordinate is the mean value of the heat transfer coefficient and the abscissa is the radial direction. The jet air flow will cause a strong interaction between the gas and solid phases near the orifice, so the solid fraction near the jet hole is minimal. As can be seen from Fig. 9 (a), the heat transfer coefficient near the orifice is minimized. The particles move upwards from the center of the fluidized bed and circulate down the wall, resulting in an increase in the heat transfer coefficient near the wall. Fig. 9

(a) also shows that at a height of 0.135 m, according to Yang and Keairns (Yang and Keairns, 1979) jet depth theory, the jet penetration depth is 0.180 m. Hence Fig. 9 (a) is still below the jet penetration depth. Here, the heat transfer coefficient increases after adding electrostatic charges, indicating that particles concentration within the bubble increases by electrostatic effect. And due to the introduction of electrostatic force, an additional force is needed to balance the electrostatic force, so particle concentration increases in the bottom. Fig. 9 (b) illustrates the change in the heat transfer coefficient at $y$ = 0.405 m. When $x$ = 0.123 m to 0.453 m, local heat transfer coefficient with $q_m$ = -0.8 μC / kg is the smallest, however, it increases near the wall.

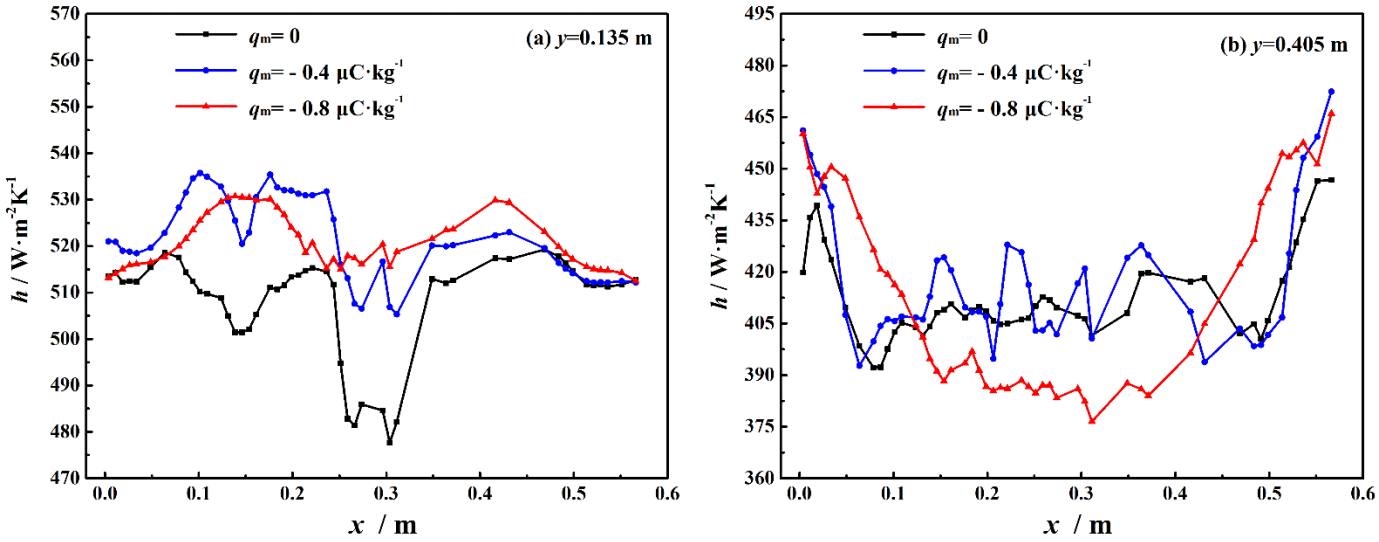


**Fig. 9 Average local heat transfer coefficient along the lateral direction**

As depicted in Fig. 9, local heat transfer coefficient at the bottom and middle of the fluidized bed actually reflects the transition of flow pattern. When the specific charge is small, the local heat transfer coefficient at the bottom of the bed increases significantly, but changes little in the upper part of the fluidized bed. However, as the specific charge increases, the particle motion becomes more disorderly or chaotic, and the asymmetric distribution of the local heat transfer coefficient also reflects the anisotropy of the fluid flow. The effect of electrostatics on the local heat transfer coefficient is very obvious. For instance, heat transfer coefficient is larger close to the wall, and solid fraction here is also high, whereas slow particle velocity may lead to local hot spots, resulting in wall sheet. However, the overall average of local heat transfer coefficient is significant,

where for $q_m$ = -0.4 and -0.8 μC / kg, the averages are 404.19 W / $m^2$K, 432.51 W / $m^2$K and 438.99 W / $m^2$K, respectively, , increased by 6.9% and 8.4%, respectively compared to uncharged system.

## 4. Conclusion

In this paper, Eulerian-Eulerian two-fluid model based on KTGF is used to investigate the effect of electrostatics on the bubble characteristics, particle fluctuation characteristics and chaotic characteristics in the gas-solid fluidized bed containing Geldart B ($d_p$ = 500 μm). After the particles are charged, the bubble frequency and bubbles number, Reynolds stress and phase space reconstruction and other parameters are significantly different from these without charges. According to the numerical simulation results, the following conclusions can be drawn:

When the particles are charged, the solids in the particle vortex are more likely to be entrained and enriched, so the solid fraction near the central axis increases. There is a strong bubble interaction region near the central axis, and its internal particles move towards the dead zone near the wall. In the transition zone between the two regions, the repulsive force between the same charged particles increases the porosity and the dead zone near the wall. And bubble diameter is significantly reduced and the bubbles are significantly elongated in the axial direction compared to these in the uncharged system.

The particle fluctuation strength also decreases, specially at the lower part of the fluidized bed reactor. With the increase of specific charges, in the lower part of the bed near the wall, bubbles reduce and the particles turbulence decline, showing that electrostatic charge is not conducive to of the particles mixing in these regions.

When particles are not charged, jet region, bubble growth region and free space region are observed in the granular temperature profile. Due to the decrease in the particle fluctuation velocity in charged system, granular temperature reduces.

Finally, the gas interchange and interphase heat transfer coefficient from bubble to emulsion phase are calculated based on the corrected throughflow velocity. Local heat transfer coefficient profiles are also calculated to estimate the overall heat transfer ability. In the future work, pressure signal collection and Particle Image Velocimetry experiment should be carried out. In the industrial production process, there are often multi-particle size distribution and charge distribution with the reactor. Thus, these parameters should be taken into consideration in the following work

## Acknowledgement

This work was supported by the Project of National Natural Science Foundation of China (No. 91434205), the National Science Fund for Distinguished Young Scholar (No. 21525627), the Science Fund for Creative Research Groups of National Nature Science Foundation of China (No.61621002), and the Fundamental Research Funds for the Central Universities (No.2017QNA4029).

## List of Symbols

$C_D$ drag coefficient

$D$ electric displacement

$D_a$ equivalent bubble diameter

$E$ electric field intensity

$f_b$ bubble frequency

$g$ gravitational acceleration

$h$ local heat transfer coefficient

$H_{be}$ interphase heat transfer coefficient

$H_s$, $H_g$ enthalpy of the solid phase and gas phase

$P$ induced polarization

$q_{be}$ gas interchange

$q_m$ specific charge

Re Reynolds number

Nu Nusselt number

$u_{bh}$, $u_{bv}$ horizontal and vertical bubble velocity

$u_{gh}$, $u_{gv}$ horizontal and vertical gas velocity

$u_{s,}$ $u_g$ velocity of the solid phase and gas phase

$u_{px}$,$u_{py}$ particle velocity in $x$ direction and $y$ direction

$U_{th}$ throughflow velocity

$U^*$ corrected velocity

$V_{jet}$ jet velocity

$\alpha_{s,}$ $\alpha_g$ volume fraction of the solid phase and gas phase

$\beta_{gs}$ momentum exchange coefficient

$\rho_{s,}$ $\rho_g$ density of fluid of solid phase and gas phase

$\chi_e$ electric susceptibility

$\in_m$ relative permittivity

$\varphi$ electrostatic potential

$\theta_{laminar}$ laminar granular temperature

$\overline{\overline{\tau}}$ stress tensor of phase $k$

$\tau_{nx}$ , $\tau_{ny}$ lateral Reynold stress and axial Reynold stress

$\Theta_s$ granular temperature

$k_{\Theta s}$ diffusion coefficient for granular energy

$\gamma_{\Theta s}$ collisional dissipation of energy

Acosta-Iborra, A., Sobrino, C., Hernandez-Jimenez, F., de Vega, M., 2011. Experimental and computational study on the bubble behavior in a 3-D fluidized bed. Chemical Engineering Science 66, 3499-3512.

Bouillard, J.X., Gidaspow, D., Lyczkowski, R.W., 1991. Hydrodynamics of fluidization-fast-bubble simulation in a 2-dimensional fluidized-bed. Powder Technology 66, 107-118.

Chalermsinsuwan, B., Gidaspow, D., Piumsomboon, P., 2014. In-depth system parameters of transition flow pattern between turbulent and fast fluidization regimes in high solid particle density circulating fluidized bed reactor. Powder Technology 253, 522-536.

Chang, J., Zhao, J., Zhang, K., Gao, J., 2016. Hydrodynamic modeling of an industrial turbulent fluidized bed reactor with FCC particles. Powder Technology 304, 134-142.

Chen, A., Bi, H.T., Grace, J.R., Kleijn van Willigen, F., Ruud van Ommen, J., 2006. Measurement of charge

distribution around a rising bubble in a 2-D fluidized bed. AIChe Journal 52, 174-184.
Chen, X., Wang, J., 2014. A comparison of two-fluid model, dense discrete particle model and CFD-DEM method for modeling impinging gas–solid flows. Powder Technology 254, 94-102.
Chiesa, M., Mathiesen, V., Melheim, J.A., Halvorsen, B., 2005. Numerical simulation of particulate flow by the Eulerian–Lagrangian and the Eulerian–Eulerian approach with application to a fluidized bed. Computers & Chemical Engineering 29, 291-304.
Cody, G.D., Goldfarb, D.J., Storch, G.V., Norris, A.N., 1996. Particle granular temperature in gas fluidized beds. Powder Technology 87, 211-232.
Davidson, J.F., Harrison, D., 1963. Fluidised particles. Cambridge University Press, Cambridge.
Dong, K., Zhang, Q., Huang, Z., Liao, Z., Wang, J., Yang, Y., 2015a. Experimental investigation of electrostatic effect on bubble behaviors in gas-solid fluidized bed. AIChe Journal 61, 1160-1171.
Dong, K., Zhang, Q., Huang, Z., Liao, Z., Wang, J., Yang, Y., Wang, F., 2015b. Experimental investigation of electrostatic effect on particle motions in gas-solid fluidized beds. AIChe Journal 61, 3628-3638.
Fang, W., Jingdai, W., Yongrong, Y., 2008. Distribution of Electrostatic Potential in a Gas−Solid Fluidized Bed and Measurement of Bed Level. Industrial & Engineering Chemistry Research 47, 9517-9526.
Gera, D., Gautam, M., 1994. Effect of voidage variation and bubble aspect ratio on throughflow in 2-D elliptical bubbles. Powder Technology 79, 159-165.
Gunn, D.J., 1978. Transfer of heat or mass to particles in fixed and fluidised beds. International Journal of Heat and Mass Transfer 21, 467-476.
Hassani, M.A., Zarghami, R., Norouzi, H.R., Mostoufi, N., 2013. Numerical investigation of effect of electrostatic forces on the hydrodynamics of gas–solid fluidized beds. Powder Technology 246, 16-25.
Hernández-Jiménez, F., García-Gutiérrez, L.M., Soria-Verdugo, A., Acosta-Iborra, A., 2015. Fully coupled TFM-DEM simulations to study the motion of fuel particles in a fluidized bed. Chemical Engineering Science 134, 57-66.
Hernandez-Jimenez, F., Gomez-Garcia, A., Santana, D., Acosta-Iborra, A., 2013. Gas interchange between bubble and emulsion phases in a 2D fluidized bed as revealed by two-fluid model simulations. Chemical Engineering Journal 215, 479-490.
Jalalinejad, F., Bi, X.T., Grace, J.R., 2012. Effect of electrostatic charges on single bubble in gas–solid fluidized beds. International Journal of Multiphase Flow 44, 15-28.
Johnson, P.C., Jackson, R., 2006. Frictional–collisional constitutive relations for granular materials, with application to plane shearing. Journal of Fluid Mechanics 176, 67-93.
Jung, J., Gidaspow, D., Gamwo, I.K., 2006. Bubble computation, granular temperatures, and reynolds stresses. Chemical Engineering Communications 193, 946-975.
Kleijn van Willigen, F., van Ommen, J.R., van Turnhout, J., van den Bleek, C.M., 2005. Bubble size reduction in electric-field-enhanced fluidized beds. Journal of Electrostatics 63, 943-948.
Knowlton, T.M., Karri, S.B.R., Issangya, A., 2005. Scale-up of fluidized-bed hydrodynamics. Powder Technology 150, 72-77.
Kolehmainen, J., Ozel, A., Boyce, C.M., Sundaresan, S., 2016. A hybrid approach to computing electrostatic forces in fluidized beds of charged particles. AIChe Journal 62, 2282-2295.
Kolehmainen, J., Ozel, A., Boyce, C.M., Sundaresan, S., 2017. Triboelectric charging of monodisperse particles in fluidized beds. AIChe Journal 63, 1872-1891.
Kuipers, J.A.M., Prins, W., Van Swaaij, W.P.M., 1991. Theoretical and experimental bubble formation at a single orifice in a two-dimensional gas-fluidized bed. Chemical Engineering Science 46, 2881-2894.
Kuipers, J.A.M., Tammes, H., Prins, W., van Swaaij, W.P.M., 1992. Experimental and theoretical porosity

profiles in a two-dimensional gas-fluidized bed with a central jet. Powder Technology 71, 87-99.
Kumar, A., Das, S., Fabijanic, D., Gao, W., Hodgson, P., 2013. Bubble-wall interaction for asymmetric injection of jets in solid–gas fluidized bed. Chemical Engineering Science 101, 56-68.
Lun, C.K.K., Savage, S.B., Jeffrey, D.J., Chepurniy, N., 1984. Kinetic theories for granular flow: inelastic particles in couette flow and slightly inelastic particles in a general flowfield. Journal of Fluid Mechanics 140, 223-256.
Lungu, M., Wang, H., Wang, J., Yang, Y., Chen, F., 2016. Two-Fluid Model Simulations of the National Energy Technology Laboratory Bubbling Fluidized Bed Challenge Problem. Industrial & Engineering Chemistry Research 55, 5063-5077.
Lungu, M., Wang, J., Yang, Y., 2015. Numerical simulations of flow structure and heat transfer in a central jet bubbling fluidized bed. Powder Technology 269, 139-152.
Nieuwland, J.J., Annaland, M.V., Kuipers, J.A.M., vanSwaaij, W.P.M., 1996a. Hydrodynamic modeling of gas/particle flows in riser reactors. AIche Journal 42, 1569-1582.
Nieuwland, J.J., Veenendaal, M.L., Kuipers, J.A.M., Van Swaaij, W.P.M., 1996b. Bubble formation at a single orifice in gas-fluidised beds. Chemical Engineering Science 51, 4087-4102.
Patil, A.V., Peters, E.A.J.F., Kolkman, T., Kuipers, J.A.M., 2014. Modeling bubble heat transfer in gas–solid fluidized beds using DEM. Chemical Engineering Science 105, 121-131.
Patil, D.J., Annaland, M.V., Kuipers, J.A.M., 2003. Gas Dispersion and Bubble-to-Emulsion Phase Mass Exchange in a Gas-Solid Bubbling Fluidized Bed: A Computational and Experimental Study. International Journal of Chemical Reactor Engineering 1.
Patil, D.J., van Sint Annaland, M., Kuipers, J.A.M., 2005. Critical comparison of hydrodynamic models for gas–solid fluidized beds—Part I : bubbling gas–solid fluidized beds operated with a jet. Chemical Engineering Science 60, 57-72.
Rokkam, R.G., Fox, R.O., Muhle, M.E., 2010. Computational fluid dynamics and electrostatic modeling of polymerization fluidized-bed reactors. Powder Technology 203, 109-124.
Sun, J., Wang, J., Yang, Y., Zhu, Z., 2015. Effects of external electric field on bubble and charged particle hydrodynamics in a gas–solid fluidized bed. Advanced Powder Technology 26, 563-575.
Sun, J., Yan, Y., 2016. Characterization of Flow Intermittency and Coherent Structures in a Gas–Solid Circulating Fluidized Bed through Electrostatic Sensing. Industrial & Engineering Chemistry Research 55, 12133-12148.
Sun, J., Yan, Y., 2017. Non-intrusive characterisation of particle cluster behaviours in a riser through electrostatic and vibration sensing. Chemical Engineering Journal 323, 381-395.
Sun, J., Zhou, Y., Ren, C., Wang, J., Yang, Y., 2011. CFD simulation and experiments of dynamic parameters in gas–solid fluidized bed. Chemical Engineering Science 66, 4972-4982.
Valenzuela, J.A., Glicksman, L.R., 1985. Gas flow distribution in a bubbling fluidized bed. Powder Technology 44, 103-113.
van der Schaaf, J., Schouten, J.C., Johnsson, F., van den Bleek, C.M., 2002. Non-intrusive determination of bubble and slug length scales in fluidized beds by decomposition of the power spectral density of pressure time series. International Journal of Multiphase Flow 28, 865-880.
Yang, W.-c., 2003. Handbook of fluidization and fluid-particle systems. CRC press.
Yang, W.-C., Keairns, D.L., 1979. Estimating the Jet Penetration Depth of Multiple Vertical Grid Jets. Industrial & Engineering Chemistry Fundamentals 18, 317-320.
Yao, L., Bi, H.T., Park, A.-H., 2002. Characterization of electrostatic charges in freely bubbling fluidized beds with dielectric particles. Journal of Electrostatics 56, 183-197.

Yusuf, R., Halvorsen, B., Melaaen, M.C., 2012. An experimental and computational study of wall to bed heat transfer in a bubbling gas–solid fluidized bed. International Journal of Multiphase Flow 42, 9-23.
Zi, C., Sun, J., Yang, Y., Huang, Z., Liao, Z., Wang, J., Yang, Y., Han, G., 2017. CFD simulation and hydrodynamics characterization of solids oscillation behavior in a circulating fluidized bed with sweeping bend return. Chemical Engineering Journal 307, 604-620.